Semiautomatic Nonrigid Registration for the Prostate and Pelvic MR Volumes[1]

Baowei Fei, PhD, Jeffrey L. Duerk, PhD, D. Bruce Sodee, MD, David L. Wilson, PhD

Rationale and Objectives. Three-dimensional (3D) nonrigid image registration for potential applications in prostate cancer treatment and interventional magnetic resonance (iMRI) imaging–guided therapies were investigated.

Materials and Methods. An almost fully automated 3D nonrigid registration algorithm using mutual information and a thin plate spline (TPS) transformation for MR images of the prostate and pelvis were created and evaluated. In the first step, an automatic rigid body registration with special features was used to capture the global transformation. In the second step, local feature points (FPs) were registered using mutual information. An operator entered only five FPs located at the prostate center, left and right hip joints, and left and right distal femurs. The program automatically determined and optimized other FPs at the external pelvic skin surface and along the femurs. More than 600 control points were used to establish a TPS transformation for deformation of the pelvic region and prostate. Ten volume pairs were acquired from three volunteers in the diagnostic (supine) and treatment positions (supine with legs raised).

Results. Various visualization techniques showed that warping rectified the significant pelvic misalignment by the rigid-body method. Gray-value measures of registration quality, including mutual information, correlation coefficient, and intensity difference, all improved with warping. The distance between prostate 3D centroids was 0.7 ± 0.2 mm after warping compared with 4.9 ± 3.4 mm with rigid-body registration.

Conclusion. Semiautomatic nonrigid registration works better than rigid-body registration when patient position is changed greatly between acquisitions. It could be a useful tool for many applications in the management of prostate.

Key Words. Automatic nonrigid image registration; mutual information (MI); thin plate spline (TPS); interventional magnetic resonance imaging (MRI); prostate cancer.

© AUR, 2005

We are investigating three-dimensional (3D) nonrigid image registration to be used in applications of prostate cancer diagnosis, staging, and therapy. In particular, we are interested in applications related to the minimally invasive interventional magnetic resonance imaging (iMRI)-guided treatment of patients with prostate cancer. At our institution, we currently use interventional MRI on a low-field open-magnet system to guide radiofrequency (RF) thermal ablation of abdominal cancer (1–3), and we are investigating this method for prostate cancer treatment.

Several applications in prostate imaging require registration. First, comparison of registered MR images acquired before and immediately after RF ablation can be used to determine whether a tumor is adequately treated. This is particularly helpful in instances in which the edematous response to treatment can be confused with a highly perfused tumor. Second, other treatment methods,

such as radiation therapy, brachytherapy, and surgery, also will be aided by registration of images from pretherapy, intratherapy, and posttherapy for treatment planning, guidance, and assessment. Third, registration of serial examinations can be used to follow up the regression or progression of tumors.

There are challenges to pelvis and prostate registration. First, pelvic regions can change shape significantly. Different patient positions, such as legs up and down, can cause movement and deformation of internal organs. Second, the normal prostate is a small organ that, when healthy, measures only about 3.8 cm in its widest dimension transversely across the base (4). Third, the small prostate is located below a much larger bladder, which can change shape and size. The prostate might move relative to the pelvic bones because of changes in bladder and rectal filling (5). Some reports described methods for image registration in the pelvis or prostate (5–18). Some of these methods require either segmentation or visual identification of structures. For example, manual registration has been used, in which an operator cues on segmented vascular structures (19), other anatomic landmarks (6,20,21), or fiducial markers (15). Others have used automated 3D schemes that match contours of bones and sometimes other structures that are extracted using manual or interactive segmentation (8,9,22). Manual segmentation also has been used to create surfaces for automatic registration (10,11).

We previously described a rigid-body volume-to-volume registration method for pelvic and prostate MR images (23). For volume pairs acquired during a short time span with the volunteer in a similar position, rigid-body registration accuracy of both the prostate centroid (typically <1 mm) and bony landmarks (average, 1.6 mm) was on the order of a voxel ($\approx$1.4 mm). With rigid-body registration, we obtained larger prostate centroid displacements (2.8–10.0 mm) when acquisitions were obtained under much different conditions (eg, legs flat and legs raised), giving large anatomic deformations. Rigid-body registration of the pelvis is inadequate under such conditions (23).

Nonrigid registration is a solution, and there are a number of relevant reports on the pelvis and prostate (24–29). Nonrigid registration methods also were used for the brain (30–32), breast (33–35), lung (36,37), and abdomen (38,39). We reported a nonrigid registration method that used many manually selected control points (CPs) (26). After automatic global rigid-body registration, the operator manually selected more than 180 CPs at the

prostate center, pelvic surface, and internal structures. The program automatically optimized each CP location by displacing it in the x, y, and z directions with respect to the reference volume until mutual information computed over a small cube of voxels was maximized. Thin plate spline (TPS) transformation then was applied to express deformation of the pelvic region and prostate. This interactive method was applied to pelvic MR images and lung computed tomographic/positron emission tomographic images (37). The time required for CP selection was a limitation.

In this study, we build on our previous experience and develop an almost fully automatic nonrigid registration method. Our goal is to automate the algorithm to save time and labor without losing registration quality. We use image data that show considerable deformation, eg, images acquired in the diagnostic (supine) and treatment positions (supine with legs raised). We qualitatively and quantitatively compare results of the new nonrigid registration algorithm with those of the previous, more manual version and rigid-body registration.

MATERIALS AND METHODS

MRI

All MRI volumes were acquired using a 1.5-Tesla Siemens MRI system (Magnetom Symphony; Siemens Medical Systems, Erlangen, Germany). An eight-element phased-array body coil was used to ensure coverage of the prostate with uniform sensitivity. Typically, two anterior and two posterior elements were enabled for signal acquisition. We used two different MR sequences. First, we used a 3D RF spoiled gradient echo steady-state pulse sequence (FLASH) with repetition time/echo time/flip parameters of 12/5.0/60, which give $256 \times 256 \times 128$ voxels over a $330 \times 330 \times 256$-mm field of view (FOV) to yield $1.3 \times 1.3 \times 2.0$-mm voxels oriented to give the highest resolution for transverse slices. Acquisition time was 5.6 minutes. This sequence was good for pelvic imaging, but was not ideal for the prostate. It was used for volunteer S1. Second, we used a 3D rapid gradient echo sequence (PSIF) designed to acquire the spin-echo component of the steady-state response. The spin echo component formed immediately before the RF pulse and was shifted toward the prior RF pulse through appropriate gradient waveform design. The sequence with 9.4/5.0/60 (repetition time/echo time/flip) yielded $160 \times 256 \times 128$ voxels over a $219 \times 350 \times 192$-mm rectangular FOV

and $1.4 \times 1.4 \times 1.5$-mm voxels oriented to give the highest resolution for transverse slices. There was oversampling at 31% in the slice direction to reduce aliasing artifacts. Acquisition time was 4.3 minutes. Most often, we used the second sequence, which gave excellent image contrast for the prostate and its surroundings. It was used for volunteers S2 and S3.

Imaging Experiments

We acquired 3D MRI volume images from three healthy volunteers under a variety of conditions simulating anticipated conditions in diagnostic and treatment applications. In the diagnostic position, the volunteer laid supine throughout MR scanning. In the treatment position, the volunteer was supine, and his legs were supported at $30°–60°$ relative to the horizon and separated in a "V," with an angle of $60°–90°$ between the two legs. This is similar to the lithotomy position used in prostate therapies, and it should provide access for needle insertion in brachytherapy or RF thermal ablation. For each volunteer, image volumes typically were obtained on the same day within an imaging session. The coil array was centered on the prostate. All images of a volunteer were acquired using the same MRI acquisition parameters. For each volunteer, one volume was in the treatment position and the other was in the diagnostic position. We performed registration experiments using treatment-diagnosis volume pairs. For volunteers S1, S2, and S3, there were three, three, and four treatment-diagnosis volume pairs, respectively. Rigid-body and nonrigid registration were applied to each pair. Additionally, we tested the methods on 10 volume pairs obtained in the same diagnostic position.

Preprocessing

The input MR volume is a 3D MR acquisition giving $256 \times 256 \times 128$ nearly isotropic voxels over an FOV covering the entire pelvis. We create isotropic voxels of approximately 1.4 mm on a side using trilinear interpolation. We optionally bin the gray scale values of two volumes to 256; this procedure helps the algorithm perform better for such multimodality registrations as computed tomography/positron emission tomography, in which their gray scales are tremendously different (37). We use Interactive Data Language (IDL; Research System Inc, Boulder, CO) as the programming language.

Nonrigid Registration by Optimizing CPs

The various steps of the algorithm are shown in Figure 1. In the first step, we used an MI method, as previously

Create reference and floating volumes following global rigid body registration
Place five feature points (FP) at prostate center, hip joints, and femurs in both volumes
Create feature points along femur using line segment approximation
Create feature points on skin surface using the prostate center and radial lines
Initialize the size of volume of interest (VOI) centered at FP's
FOR *FP* FROM *0* to *N-1* DO BEGIN
    Optimize mutual information (MI) between the reference and floating VOI's
    1. Transform the floating VOI using three translations and three rotations
    2. Interpolate to get a reformatted VOI
    3. Calculate MI between the reference and reformatted VOI's
    4. Vary the three translation and three rotation parameters
    5. Repeat steps 1-4 until meeting function tolerance or maximum iteration number
    Record the optimized FP coordinates in the floating volume
END
Determine control points (CP) using the feature points and VOI's
Calculate thin plate spline transformation using the reference and optimized CP's
Interpolate the floating volume and get a warped volume

Figure 1. Flow chart of the nonrigid registration algorithm. The first four steps are to create FPs in both volumes after global rigid-body registration. The loop from FOR to END is to optimize VOIs as centered at corresponding FPs using MI. The optimal VOI is used to determine nine CPs that represent the position and orientation of the VOI. The position information of all CPs is used to establish a 3D TPS transformation for the entire volume. See text for details.

reported by us (23), for the rigid-body registration that captured the global transformation of two volumes. In the following sections, we mainly describe the steps of the nonrigid registration method.

Semiautomatic detection of feature points

After global transformation, we manually selected five corresponding pairs of feature points (FPs; Figure 2) from the two volumes. Locations are the prostate center (FP0), two hip joints (FP1 and FP2), and two distal femurs (FP3 and FP4). Transverse slices are used to select these points because they better show displacement of the legs. We first selected FP0, FP1, and FP2. Starting from the slice with FP1, we browsed images slice by slice toward the
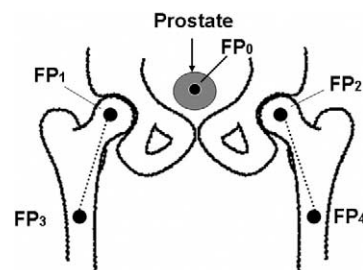

Figure 2. Locations of the manually selected five FPs. FP0 is at the prostate center; FP1 and FP2, hip joints; and FP3 and FP4, distal femurs. Dash lines connecting FP1 and FP3 and FP2 and FP4 are along the femurs.
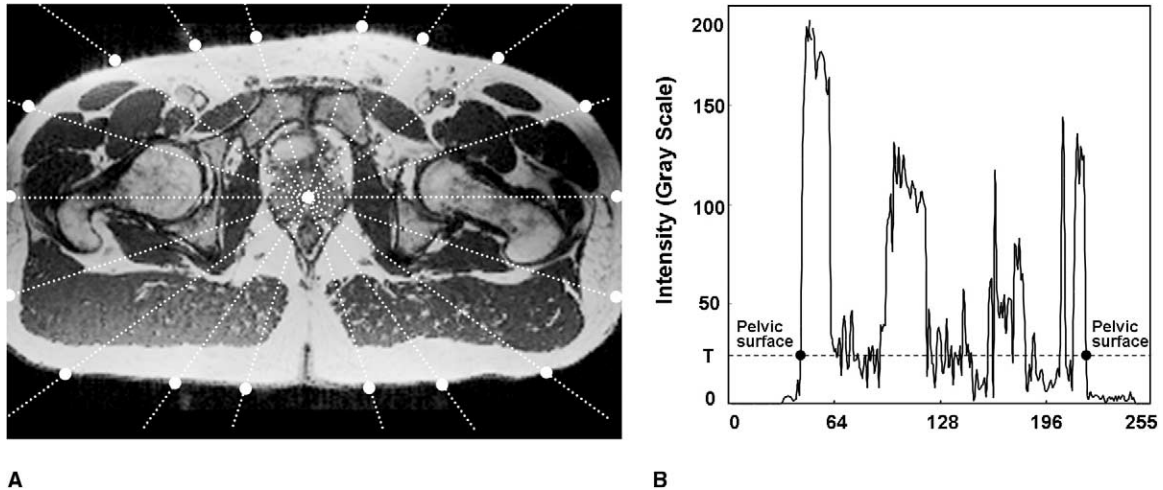
Figure 3. Automatic detection of the pelvic surfaces. (a) A transverse image slice covering the prostate. Dash lines pass thought the prostate with an equal angle increment, dots are at the pelvic exterior surfaces. (b) Graph plots the intensity signals along one dash line in (a). A threshold, T, is used to determine pelvic surfaces along this line.

foot. After 40 transverse slices (∼56 mm) away from FP1, we located FP3 and placed the FP at the femur center. We used a similar method to select FP4. Because of subsequent optimization later, point pairs do not have to exactly lie on corresponding features; an error of up to 15 mm or ≈10 voxels is well tolerated. These FPs are especially useful when registering volumes obtained in the diagnostic (supine) and treatment (supine with legs raised) positions (23,26). Images from both volumes are shown side by side to aid interpretation.

Using these five FPs, the program creates all other FPs automatically. First, for each volume, a line segment is created between FPs at the hip joint and distal femur (dashed lines, Figure 2). Each segment is divided into eight equal lengths to obtain seven additional FPs. Altogether, we obtained nine corresponding FP pairs for each femur.

Second, the prostate center is used to create FPs at the pelvic surfaces (Figure 3a). Many radial lines are drawn through the prostate center in a two-dimensional transverse slice. The angle between lines, the angle increment, normally was 18°, 20°, or 30°. Note that we exclude the vertical line because it normally intersects the buttock groove and/or penis, regions of relatively little interest that can change considerably from one acquisition to the next. The gray-scale intensity of the pixels along each line is obtained (Figure 3b). The signal in air is noise and normally less than 15 gray levels compared with a mean signal of approximately 90 and maximum signal of approximately 500 in the tissues. The pelvic skin surface

gives high-intensity signals, greater than 30 gray levels, because of fat beneath the skin. We searched each line for the most distant point above a threshold, T (Figure 3b) and set this position to be a surface FP (Figure 3a). To smooth intensities along each line, a median filter is applied optionally to improve the detection of surface points. For scaled intensities of 0–255, we normally choose a threshold of 20 gray levels. After processing all lines in an image slice, the program repeats the procedure for four other transverse slices that are selected with a gap of approximately 10 mm away from each other. These transverse slices span ≈40 mm, much of a typical prostate.

For a typical registration with an angle increment of 18°, there are 91 pairs of FPs: one at the prostate center, 18 at the femurs, and 72 at the exterior pelvic surface. Their 3D coordinates are stored.

Optimization of Corresponding FPs

Corresponding FPs are optimized by using a mutual information similarity measure (26). A small cubic volume of interest (VOI) is centered at each FP. The VOI can be 32, 48, or 64 voxels on a side, and, as reported later, selection of VOI size depends on the amount of warping required. In both the reference and floating volumes, each corresponding FP has its own VOI. The one in the reference volume is the reference VOI that is known and fixed. The corresponding VOI in the floating volume is the floating VOI. The X, Y, and Z axes are defined along left-right, anterior-posterior, and cranial-
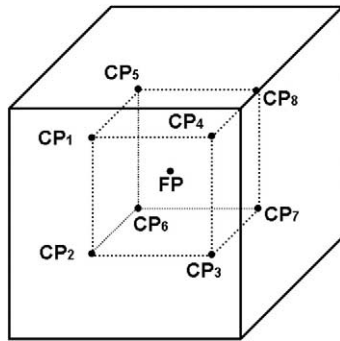
Figure 4. Nine CPs for each FP and VOI. The big cubic volume is the VOI used to calculate MI and optimize the FP. The small cubic volume is with the same center and orientation, but half size on a side. The center and eight corners of the smaller cubic volume are the CPs that will be used to establish TPS transformation.

caudal directions, respectively. The origin is located at the center of the FP. To perform rigid-body optimization, we translate and rotate the floating VOI with respect to the reference VOI and compute their MI over corresponding voxels. There are six transformation parameters to optimize: three displacements in x, y, and z and three angles about each of these three axes. We used the Nelder-Mead Simplex algorithm (40) for optimization.

Optimal transformation parameters are independently obtained and recorded for each floating FP. On rare occasions, one or more of the translation or rotation parameters of a floating FP are larger than a reasonable value (eg, 40 mm or 45°), and we eliminate it.

Determination of CPs

For each optimized FP VOI, we create nine optimal CPs. As shown in Figure 4, there is a smaller cube approximately half the dimensions of a bigger cube that is used to compute MI. The nine CPs are the eight corners and the center of the small cube. These CPs encode the position and orientation of the VOI. For FPs near the MR image volume border, some CPs may not be in the volume, and we exclude them. The total number of CPs usually is >600 for an angle increment of 18°.

TPS transformation using optimal points

The final major step is to obtain the warped volume from the floating volume. We used backward warping that includes two steps to obtain the warped volume (41). The first step is a spatial transformation that maps each voxel in the target image to its source in the source image

(41). We use the optimal coordinates of CPs to establish a 3D TPS transformation (42,43) between the floating (source) and warped (target) image volumes. For example, a voxel with 3D coordinates of (64, 78, 24) in the target image is mapped to its source at (63.2, 76.3, 22.1). The second step is computation of the intensity value at each source location. Because the position of the source often can be real valued, for example, (63.2, 76.3, 22.1), we use trilinear interpolation to obtain its intensity value. We then copy the intensity value and assign it to the target voxel in the warped volume. Finally, we obtain the warped volume from the floating image.

We summarize parameter values for the nonrigid registration. The 3D coordinates of the five FPs are selected manually by the user. The angle increment is 18°, intensity threshold for pelvic surface detection is 20 gray scales, and VOI size is 32 or 64.

Registration Evaluation

We used multiple visualization features of RegViz, a program written in IDL and created in our laboratory for visualizing and analyzing registered image volumes. First, color overlay displays were used to evaluate overlap of structures. One image was rendered in gray and the other in the "hot-iron" color scheme available in IDL. To visualize potential differences, it was useful to interactively change the contribution of each image by using the transparency scale. Second, we used a sector display that divided the reference and registered images into rectangular sectors and created an output image by alternating sectors from the two input images. Even subtle shifts of edges could be seen clearly. Third, we manually segmented prostate boundaries in image slices and copied them to corresponding slices from the other volume. This enabled visual determination of the overlap of prostate boundaries over the entire volume. We applied the same method to evaluate pelvic registration.

Correlation coefficient (CC) and MI were calculated as indicators of registration quality. Because volumes to be registered were acquired using the same acquisition parameters, high absolute CC values were obtained when registration was good (34). Absolute CC is used, rather than MI values, because it has a well-defined range between 0 and 1 and provides an independent check of MI results.

We compared the new semiautomatic method with a nonrigid registration that used manually selected CPs, as reported by us (26). Briefly, in the previous method, we first performed a rigid-body registration, then manually
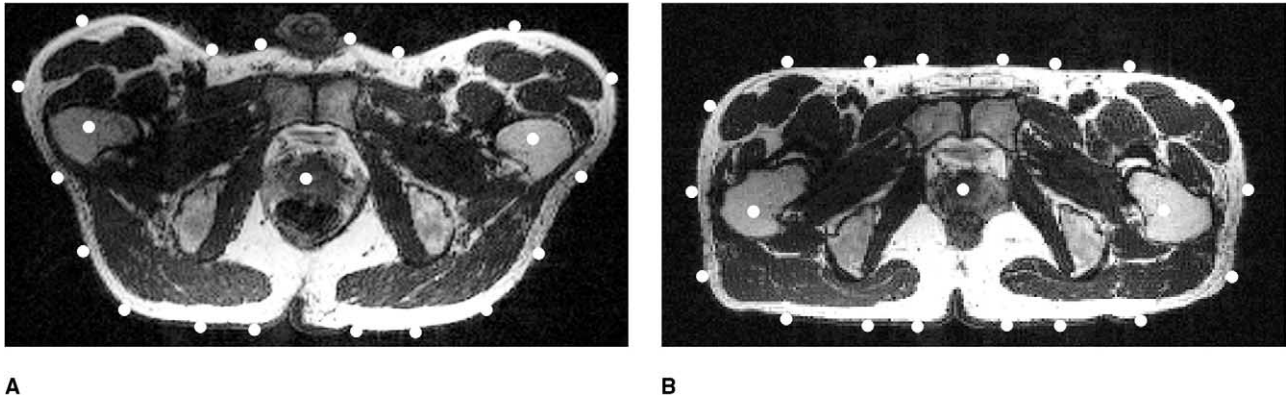
Figure 5. FPs for images acquired in the treatment and diagnostic positions; (a) from the reference volume acquired in the treatment position with legs raised, and (b) is to be warped and is from the volume acquired in the diagnostic position with legs flat on the table. FPs are located at the prostate center, femurs, and pelvic surfaces. Each FP is located at one voxel, but displayed much larger for improved visualization. Volumes are of volunteer S2.

selected about 180 CPs, automatically optimized their locations, and finally warped the volume using TPS interpolation. The principal change in the current algorithm is the automation of CP selection after identification of five FPs. A rigid-body method also was described previously (23).

We measured potential displacements of the 3D centroid of the prostate to assess prostate registration error. We used RegViz to manually segment the prostate across all image slices and calculated a 3D centroid.

RESULTS

Determination of FPs

The method for finding corresponding FPs was successful. After rigid-body registration, our visualization tool made it easy to approximately locate the prostate center, hip joints, and femurs. The automatic detection method for identifying the external pelvic surface was reliable. For all volume pairs, the program correctly detected all surface points using all angle increments and a threshold of 20 gray levels. Figure 5 shows surface FPs for a typical treatment-diagnostic volume pair. The method for finding FPs along the femurs also worked in a robust fashion.

In more than 60 nonrigid registration experiments using 10 treatment-diagnosis volume pairs, we found that more FPs generally improved registration quality. Figure 6 plots MI values of registered volumes after warping as a function of angle increment. When the angle increment is less than 20°, MI saturates. As the angle increment in-

creases, less FPs are used and the MI value decreases. The downside of adding more CPs is the increased time for registration. We use an angle increment of 18° in subsequent experiments.

Adding FPs along the femurs was important for good registration of internal structures. When only surface FPs were used, the femurs and surrounding structures did not register well (not shown), even with a very large number of surface points, obtained with an angle increment of 9°. FPs along the femurs are important for satisfactory registration because those points provide the constraint for the TPS transformation and bone should not be warped. Ex-
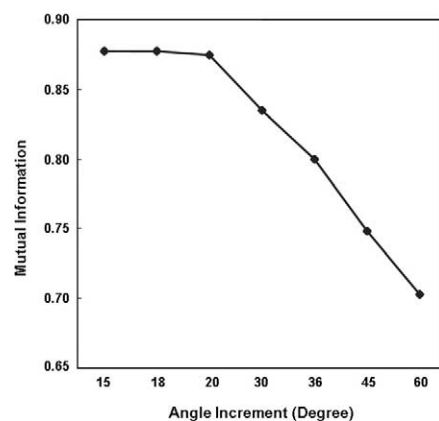

Figure 6. MI as a function of angle increment. Y-Axis, MI values between registered volumes; x-axis, angle increments used to detect pelvic surfaces. Generally, MI values decreased when angle increment increased because fewer FPs participated in nonrigid registration. MI values saturate when the angle increment is smaller than 20°. The number of FPs varied from 15 to 60 for angle increments of 107 to 43, respectively.
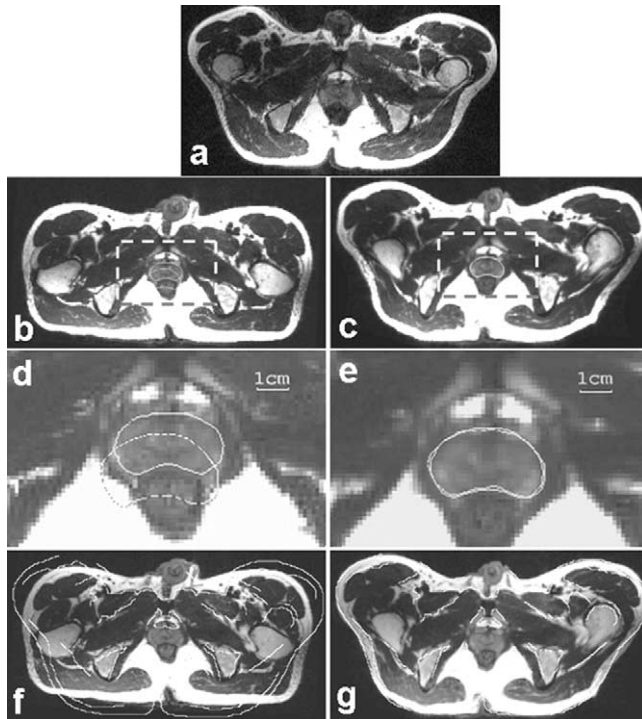
Figure 7. Comparison of nonrigid and rigid-body registration for volumes acquired in the treatment and diagnostic positions. (a) From the reference volume acquired in the treatment position, and the prostate is manually segmented. Images in the left and right columns are from the floating volume acquired in the diagnostic position after rigid-body and nonrigid registration, respectively. To show potential mismatch, the prostate contour from the reference in (a) is copied to (b) and (c) and magnified as the dashed contours in (d) and (e). (e) Movement of the prostate to the posterior is corrected with warping, but (d) not rigid-body registration. Pelvic boundaries manually segmented from the reference show (f) significant misalignment with rigid body that is (g) greatly improved with warping. All registration experiments are performed in 3D. Transverse slices covering the prostate are selected from 3D image volumes. Images are from volunteer S2.

periments showed that fewer FPs along the femurs did not satisfactorily remove deformations when the legs were raised in the treatment position.

Registration Quality of Nonrigid versus Rigid-Body Registration

In Figure 7, we compare nonrigid and rigid-body registration for a typical volume pair from the treatment and diagnostic positions. After nonrigid registration, the prostate boundary overlap is excellent (Figure 7e) and within manual segmentation error, assessed by an experienced operator. Using rigid-body registration, there is significant misalignment throughout large regions in the pelvis, as shown in the overlap image (Figure 7f), and alignment is
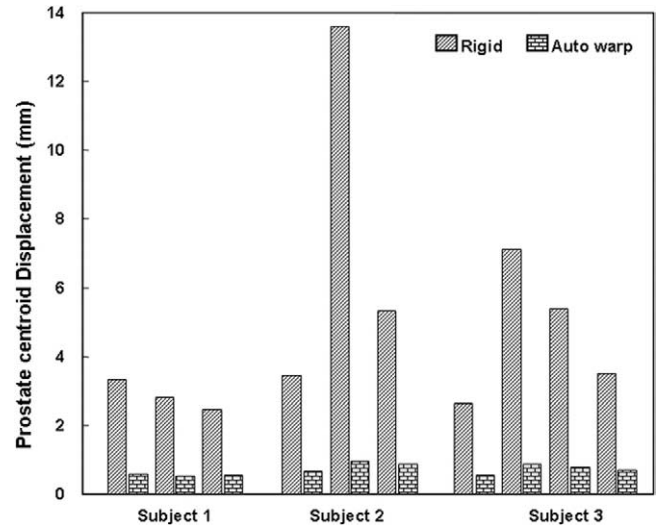

Figure 8. Prostate centroid displacement after rigid-body and nonrigid registration. Ten treatment-diagnosis volume pairs from three volunteers were registered using rigid-body and nonrigid registration, respectively. After rigid-body registration, mean displacement of prostate centroid between registered volumes was 4.9 ± 3.4 (SD) mm across all volume pairs. After warping, mean displacement was only 0.7 ± 0.2 mm. Warping significantly decreased displacement, indicating much better registration of the prostate.

improved greatly with warping (Figure 7g) in which the pelvis matched very well, even at the outer surfaces. Similar results were obtained in transverse slices throughout the prostate. Other visualization methods, such as two-color overlays and difference images (not presented), also show excellent matching of structures.

Visual inspections were verified further by quantitative measurements. Figure 8 shows prostate centroid displacement after rigid-body and nonrigid registration. Warping significantly decreased displacement, indicating much better registration of the prostate. After warping, mean displacement was only 0.7 ± 0.2 (SD) mm across all volume pairs. However, the mean was 4.9 ± 3.4 mm for rigid-body registration.

A typical example is the second pair of volunteer S2. After rigid-body registration, the prostate was misaligned, with displacement to the posterior of about 13.6 mm when in the treatment position (Figure 7d). A prostate rotation of about 14° along the left-right axis also was found after rigid-body registration. After nonrigid registration, the 3D prostates matched very well and the centroid calculated from segmented images displaced by only 0.9 mm, or 0.7 voxels.

Additionally, we examined 10 volume pairs, with both volumes acquired in the diagnostic position. In all such
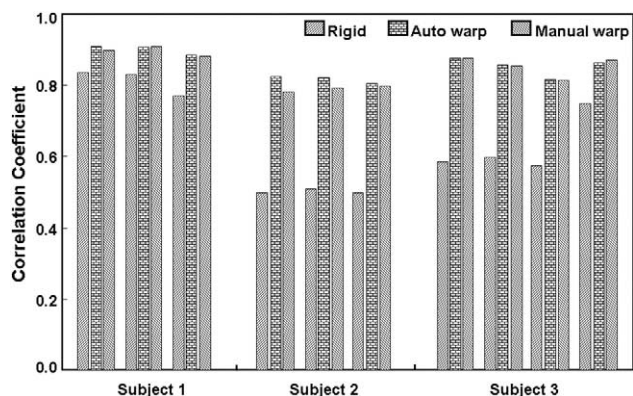
Figure 9. Comparison of rigid-body, semiautomatic, and manual nonrigid registration for treatment-diagnosis volume pairs. CCs after registration are plotted. Both semiautomatic and manual nonrigid registration increased the CC compared with rigid-body registration in each case, and this effect was significant, determined from all data ($P < .5$). The semiautomatic method is better than the manual nonrigid registration, with 180 CPs in 7 of 10 trials. There are a total of 10 volume pairs from three volunteers, as described previously.

cases, rigid-body registration worked as well as nonrigid registration. There were no noticeable deformations in the pelvic region, and prostate centroids typically displaced less than 1.0 mm between the two registered volumes. Note that this was obtained even though volunteers always got up from the table and moved around before being imaged again. In what follows, we only report results of treatment-diagnosis volume pairs.

In Figure 9, we compare rigid-body, manual warping, and our new almost fully automatic nonrigid methods. CC values between registered volumes of treatment-diagnosis are plotted. Both semiautomatic and manual nonrigid registration significantly increased CC values in every case, and a paired two-tailed t-test indicated a significant effect of warping at $P < .5$. The semiautomatic nonrigid registration worked better than the manual one in seven of 10 cases. This probably occurs because we used more (≈ 600) CPs with the semiautomated than manual method (≈ 180). Recall that with the manual method, each FP was optimized for translation and not rotation, and each FP gave one CP.

Algorithmic Implementation

We report some details on nonrigid registration for a typical volume pair from volunteer S2. The angle increment was 18°, and total number of FPs was 91. After FP optimization, 21 FPs were rejected and 70 FPs remained that produced 630 CPs. Excluding 17 invalid CPs outside

the volume region, there were 613 useful CPs for the TPS transformation. After rigid-body registration, mean distance between the reference and floating FPs was 18.6 ± 12.4 (SD) mm. Maximum distance was 58.2 mm. The maximum rotation of a VOI was 40.3°. Using a computer with 3.4-MHz central processing unit and 3 gigabyte memory, for volumes with 256 × 256 × 140 voxels, nonrigid registration took about 15 minutes, with TPS warping occupying ≈86% of the time. Very probably, the time could be improved greatly with optimized C code, rather than the high-level language, IDL.

VOI size was an important parameter to control the amount of warping. We performed experiments to find the optimal VOI size by using sizes of 16, 32, 64, and 72 voxels. We quickly found that a VOI size of 16 or 72 voxels on a side gave unsatisfactory results because warping was either too much or too little, respectively. A VOI size of 64 worked better than other VOI sizes for S1 and S3 because there was relatively little deformation between volume pairs. However, a VOI size of 32 voxels on a side performed best for volunteer S2 because there was more deformation in this case (Figure 7).

The method for obtaining CPs from FPs satisfactorily encoded the local position and orientation for warping. As described, we used the corners and center of a small cubic volume contained within the FP VOI. Using the corners of the FP VOI gave unsatisfactory results from visual inspection, as well as CC and MI values.

DISCUSSION

For MR images of the pelvis and prostate, nonrigid registration is desirable when images are acquired in different positions. Local deformations throughout the pelvis can be corrected, and, more importantly, the prostate can be accurately registered. However, when images are acquired in the same position under similar conditions, such as the case called diagnosis-diagnosis, rigid-body registration worked satisfactorily (23). Similarly, if one were to reproduce the treatment position reasonably well, one again could probably get very good results with rigid-body registration.

High-resolution MR images provide a very stringent test for warping. Many anatomic details are evident, and even a small mismatch can be seen clearly. With a sufficient number of CPs, TPS transformation excellently approximated the deformations of the pelvis and internal structures of our MR images. Even when we warped the

volume in the diagnostic position to one in the treatment position, most organs were closely aligned despite very significant movements.

With nonrigid registration, we have to be concerned about potential warping errors affecting the application of interest. For the prostate, we used only one CP at the prostate center because we desired to maintain the spatial integrity of the organ and preserve tissue volume. We placed many CPs around the pelvic surface to produce reasonable warping.

The semiautomatic method is fast and reliable. A user only needs to place five FPs in a procedure that is straightforward with our graphical user interface. All other tasks are automated. In addition, the localization error of FPs up to 15 mm or $\approx$10 voxels is well tolerated. Compared with the manual nonrigid method, the almost fully automated method saved time and labor and gave registrations that were as good as or better than the manual method. An interesting semiautomatic method was reported previously for landmark localization in the brain (29) that would be time consuming for use in the pelvis. A user manually specified a region of interest, a 3D differential operator was applied to obtain landmark candidates within the region of interest, and the user selected the most promising candidate. Unlike brain images, pelvic volume needs hundreds of points (600 in our study) to correct the huge deformation not seen in the brain.

The flexibility of the semiautomatic method makes the current software suitable for nonrigid registration in many applications, in addition to clinical procedures described previously. We believe the registration method can be applied to other modalities and intersubject images. In addition, the general approach probably can be modified for other organ systems.

The nonrigid registration algorithm is designed to be very computationally efficient for TPS warping with hundreds of CPs. We optimized each CP separately because optimization of six parameters (three translations and three rotations) is simple and fast. Simultaneous optimization of many CPs is another approach (44). However, our experiments show that 600 CPs with 1800 free parameters are needed; hence, simultaneous optimization would be extraordinarily complex and time consuming. We applied TPS transformation once to the final optimal CPs; this saved considerable time and gave satisfactory warping. If TPS was applied during each iteration of the optimization process (44), registration time would be unacceptable. If we were to use optimized C code instead of IDL, the rig-

id-body and nonrigid registration should be more time efficient.

Because there is no standard method, we used a variety of methods to evaluate nonrigid registration quality. First, for routine evaluation, a color overlay is simple, fast, and intuitive (45). To better visualize the two data sets, we interactively adjust the transparency scale of each image. Second, for illustration of subtle difference along an edge, we use a sector display because it best shows small shifts (46). Third, for visual evaluation of a specific organ, such as the prostate, we like to superimpose manually marked contours from one image onto another, as shown in Figure 7. This clearly shows any displacement or deformation. Fourth, a more quantitative approach is obtained by calculating the displacement of a 3D centroid of the segmented prostate. Finally, when images have similar gray levels, a difference image and statistics on the difference image provide yet another approach. A downside with MR images is that the inhomogeneity of the signal response and interpolation can introduce artifacts in the difference images. Because MR image intensity can vary with different MR sequence parameters and the signal response of MR coil, the gray-value statistic may have some limitations when image acquisitions are not carefully repeated. Similarly, there are other gray-level measures, such as the CC. Although the absolute value of CC and other gray-scale measures might not predict registration quality, it probably is a very good way to compare registrations on a single volume pair, as in Figure 9.

We conclude that semiautomatic nonrigid registration works better than rigid-body registration when patient position is changed greatly between acquisitions. It also compares favorably with nonrigid registration with manual selection of CPs. We believe it will be a useful tool for many applications.

REFERENCES

1. Carrillo A, Duerk JL, Lewin JS, Wilson DL. Semiautomatic 3-D image registration as applied to interventional MRI liver cancer treatment. IEEE Trans Med Imaging 2000; 19:175–185.
2. Lewin JS, Connell CF, Duerk JL, et al. Interactive MRI-guided radiofrequency interstitial thermal ablation of abdominal tumors: clinical trial for evaluation of safety and feasibility. J Magn Reson Imaging 1998; 8:40–47.
3. Merkle EM, Shonk JR, Duerk JL, Jacobs GH, Lewin JS. MR-guided RF thermal ablation of the kidney in a porcine model. AJR Am J Roentgenol 1999; 173:645–651.
4. Gray H. Anatomy, Descriptive and Surgical (The classic collector's edition). New York, NY: Gramercy, 1977:1010.
5. vanHerk M, Bruce A, Kroes APG, Shouman T, Touw A, Lebesque JV. Quantification of organ motion during conformal radiotherapy of the

prostate by three dimensional image registration. Int J Radiat Oncol Biol Phys 1995; 33:1311–1320.

6. Narayana V, Roberson PL, Winfield RJ, McLaughlin PW. Impact of ultrasound and computed tomography prostate volume registration on evaluation of permanent prostate implants. Int J Radiat Oncol Biol Phys 1997; 39:341–346.

7. van Herk M, de Munck JC, Lebesque JV, Muller S, Rasch C, Touw A. Automatic registration of pelvic computed tomography data and magnetic resonance scans including a dull circle method for quantitative accuracy evaluation. Med Phys 1998; 25:2054–2067.

8. Antolak JA, Rosen II, Childress CH, Zagars GK, Pollack A. Prostate target volume variations during a course of radiotherapy. Int J Radiat Oncol Biol Phys 1998; 42:661–672.

9. Remeijer P, Geerlof E, Ploeger L, Gilhuijs K, van Herk M, Lebesque JV. 3-D portal image analysis in clinical practice: an evaluation of 2-D and 3-D analysis techniques as applied to 30 prostate cancer patients. Int J Radiat Oncol Biol Phys 2000; 46:1281–1290.

10. Roeske JC, Forman JD, Mesina CF, et al. Evaluation of changes in the size and location of the prostate, seminal vesicles, bladder, and rectum during a course of external beam radiation therapy. Int J Radiat Oncol Biol Phys 1995; 33:1321–1329.

11. Scott AM, Macapinlac HA, Divgi CR, et al. Clinical validation of SPECT and CT/MRI image registration in radiolabeled monoclonal-antibody studies of colorectal carcinoma. J Nucl Med 1994; 35:1976–1984.

12. Reynier C, Troccaz J, Fourneret P, et al. MRI/TRUS data fusion for prostate brachytherapy. Preliminary results. Med Phys 2004; 31:1568–1575.

13. Court LE, Dong L. Automatic registration of the prostate for computed-tomography-guided radiotherapy. Med Phys 2003; 30:2750–2757.

14. Jobse M, Davelaar J, Hendriks E, Kattevilder R, Reiber H, Stoel B. A new algorithm for the registration of portal images to planning images in the verification of radiotherapy, as validated in prostate treatments. Med Phys 2003; 30:2274–2281.

15. Parker CC, Damyanovich A, Haycocks T, Haider M, Bayley A, Catton CN. Magnetic resonance imaging in the radiation treatment planning of localized prostate cancer using intra-prostatic fiducial markers for computed tomography co-registration. Radiother Oncol 2003; 66:217–224.

16. Mizowaki T, Cohen GN, Fung AY, Zaider M. Towards integrating functional imaging in the treatment of prostate cancer with radiation: the registration of the MR spectroscopy imaging to ultrasound/CT images and its implementation in treatment planning. Int J Radiat Oncol Biol Phys 2002; 54:1558–1564.

17. Ruchala KJ, Olivera GH, Kapatoes JM. Limited-data image registration for radiotherapy positioning and verification. Int J Radiat Oncol Biol Phys 2002; 54:592–605.

18. Bansal R, Staib L, Chen Z, et al. A minimax entropy registration framework for patient setup verification in radiotherapy. Comput Aided Surg 1999; 4:287–304.

19. Hamilton RJ, Blend MJ, Pelizzari CA, Milliken BD, Vijayakumar S. Using vascular structure for CT-SPECT registration in the pelvis. J Nucl Med 1999; 40:347–351.

20. Liehn JC, Loboguerrero A, Perault X, Demange L. Superimposition of computed-tomography and single photon emission tomography immunoscintigraphic images in the pelvis—validation in patients with colorectal or ovarian carcinoma recurrence. Eur J Nucl Med 1992; 19:186–194.

21. Balter JM, Sandler HM, Lam K, Bree RL, Lichter AS, Ten Haken RK. Measurement of prostate movement over the course of routine radiotherapy using implanted markers. Int J Radiat Oncol Biol Phys 1995; 31:113–118.

22. Herk MV, de Munck JC, Lebesque JV, Muller S, Rasch C, Touw A. Automatic registration of pelvic computed tomography data and magnetic resonance scans including a full circle method for quantitative accuracy evaluation. Med Phys 1998; 25:2054–2067.

23. Fei BW, Wheaton A, Lee Z, Duerk JL, Wilson DL. Automatic MR volume registration and its evaluation for the pelvis and prostate. Phys Med Biol 2002; 47:823–838.

24. Wang H, Dong L, Lii MF, et al. Implementation and validation of a three-dimensional deformable registration algorithm for targeted prostate cancer radiotherapy. Int J Radiat Oncol Biol Phys 2005; 61:725–735.

25. Lu W, Chen ML, Olivera GH, Ruchala KJ, Mackie TR. Fast free-form deformable registration via calculus of variations. Phys Med Biol 2004; 49:3067–3087.

26. Fei BW, Kemper C, Wilson DL. A comparative study of warping and rigid body registration for the prostate and pelvic MR volumes. Comput Med Imaging Graphics 2003; 27:267–281.

27. Wu X, Dibiase SJ, Gullapalli R, Yu CX. Deformable image registration for the use of magnetic resonance spectroscopy in prostate treatment planning. Int J Radiat Oncol Biol Phys 2004; 58:1577–1583.

28. Bharatha A, Hirose M, Hata N, Warfield SK, Ferrant M, Zou KH. Three-dimensional finite element-based deformable registration of pre- and intraoperative prostate imaging. Radiology 2001; 221:224–224.

29. Hirose M, Bharatha A, Hata N, et al. Quantitative MR imaging assessment of prostate gland deformation before and during MR imaging-guided brachytherapy. Acad Radiol 2002; 9:906–912.

30. Rohr K, Stiehl HS, Sprengel R, Buzug TM, Weese J, Kuhn MH. Landmark-based elastic registration using approximating thin-plate splines. IEEE Trans Med Imaging 2001; 20:526–534.

31. Christensen GE, Yin P, Vannier MW, Chao KSC, Dempsey JF, Williamson JF. Large-deformation image registration using fluid landmarks. Proceedings of 4th IEEE Southwest Symposium on Image Analysis and Interpretation 2000; 269–273, IEEE.

32. Maurer CR, Hill DLG, Martin AJ, et al. Investigation of intraoperative brain deformation using a 1.5-T interventional MR system: preliminary results. IEEE Trans Med Imaging 1998; 17:817–825.

33. Davis MH, Khotanzad A, Flamig DP, Harms SE. A physics-based coordinate transformation for 3-D image matching. IEEE Trans Med Imaging 1997; 16:317–328.

34. Rueckert D, Sonoda LI, Hayes C, Hill DLG, Leach MO, Hawkes DJ. Nonrigid registration using free-form deformations: application to breast MR images. IEEE Trans Med Imaging 1999; 18:712–721.

35. Denton ERE, Sonoda LI, Rueckert D, et al. Comparison and evaluation of rigid, affine, and nonrigid registration of breast MR images. J Comput Assist Tomogr 1999; 23:800–805.

36. Zhang T, Orton NP, Mackie TR, Paliwal BR. Technical note: a novel boundary condition using contact elements for finite element based deformable image registration. Med Phys 2004; 31:2412–2415.

37. Lee Z, Kemper C, Muzic R, Berridge MS, Wilson DL. Quantitative pulmonary imaging based on PET-CT co-registration with warping. J Nucl Med 2001; 42:10–11.

38. Christensen GE, Rabbitt RD, Miller MI. Deformable templates using large deformation kinematics. IEEE Trans Image Processing 1996; 5:1435–1447.

39. Wilson DL, Carrillo A, Zheng L, Genc A, Duerk JL, Lewin JS. Evaluation of 3D image registration as applied to MR-guided thermal treatment of liver cancer. J Magn Reson Imaging 1998; 8:77–84.

40. Nelder J, Mead RA. A simplex method for function minimization. Comput J 1965; 7:308–313.

41. Gomes J, Costa B, Darsa L, Velho L. Warping and Morphing of Graphical Objects. Silicon Valley, CA: Morgan Kaufman, 1999.

42. Goshtasby A. Registration of images with geometric distortions. IEEE Trans Geoscience Remote Sensing 1988; 26:60–64.

43. Bookstein FL. Principal warps—thin-plate splines and the decomposition of deformations. IEEE Trans Pattern Analysis Machine Intell 1989; 11:567–585.

44. Meyer CR, Boes JL, Kim B, et al. Demonstration of accuracy and clinical versatility of mutual information for automatic multimodality image fusion using affine and thin-plate spline warped geometric deformations. Med Image Analysis 1996; 1:195–206.

45. Fei BW, Lee Z, Duerk JL, Lewin JS, Sodee DB, Wilson DL. Registration and fusion of SPECT, high resolution MRI, and interventional MRI for thermal ablation of the prostate cancer. IEEE Trans Nucl Sci 2004; 51:177–183.

46. Fei BW, Duerk JL, Boll DT, Lewin JS, Wilson DL. Slice to volume registration and its potential application to interventional MRI guided radiofrequency thermal ablation of prostate cancer. IEEE Trans Med Imaging 2003; 22:515–525.

Fei BW, Duerk JL, Sodee DB, Wilson DL. Semiautomatic nonrigid registration for the prostate and pelvic MR volumes. Academic Radiology 2005;12:815-824.